



**HAL**  
open science

## Multifunctionality of weak ferromagnetic porphyrin-based MOF: selective adsorption in liquid and gas phase

Eder Amayuelas, Paul Iacomi, Arkaitz Fidalgo-Marijuan, Begoña Bazán, Miren Karmele Urtiaga, Gotzone Barandika, Luis Lezama, Philip Llewellyn, María Isabel Arriortua

### ► To cite this version:

Eder Amayuelas, Paul Iacomi, Arkaitz Fidalgo-Marijuan, Begoña Bazán, Miren Karmele Urtiaga, et al.. Multifunctionality of weak ferromagnetic porphyrin-based MOF: selective adsorption in liquid and gas phase. *CrystEngComm*, 2021, 23 (23), pp.4205-4213. 10.1039/D1CE00046B . hal-03662699

**HAL Id: hal-03662699**

**<https://amu.hal.science/hal-03662699>**

Submitted on 9 May 2022

**HAL** is a multi-disciplinary open access archive for the deposit and dissemination of scientific research documents, whether they are published or not. The documents may come from teaching and research institutions in France or abroad, or from public or private research centers.

L'archive ouverte pluridisciplinaire **HAL**, est destinée au dépôt et à la diffusion de documents scientifiques de niveau recherche, publiés ou non, émanant des établissements d'enseignement et de recherche français ou étrangers, des laboratoires publics ou privés.

## Multifunctionality of weak ferromagnetic porphyrin-based MOF: selective adsorption in liquid and gas phase

Eder Amayuelas,<sup>\*a</sup> Paul Iacomí,<sup>\*b</sup> Arkaitz Fidalgo-Marijuan,<sup>c</sup> Begoña Bazán,<sup>a,c</sup> Miren Karmele Urtiaga,<sup>a</sup> Gotzone Barandika,<sup>c,d</sup> Luis Lezama,<sup>d</sup> Philip L. Llewellyn<sup>b</sup> and María Isabel Arriortua.<sup>a,c</sup>

Received 00th January 20xx,  
Accepted 00th January 20xx

DOI: 10.1039/x0xx00000x

In the endless possibility space of metal organic framework design, the quest for new multifunctional materials with desirable properties is still ongoing. At the environmental level, their development poses a promising industrial alternative for the management of aqueous pollutants and for storage and separation of gases. In this context, the recently reported porphyrinic framework **1**, [Ni<sub>5</sub>(H<sub>2</sub>TCP)<sub>2</sub>O(H<sub>2</sub>O)<sub>4</sub>]<sub>n</sub>S (where H<sub>6</sub>TCP is meso-tetra(4-carboxyphenyl)porphyrin and S is the solvent) is investigated through a fundamental study of its thermal and magnetic properties, together with its potential as an adsorbent for pollutants in the liquid and gas phase. Sorption of four organic dye solutions with different chemical features was carried out, with good affinity found towards small cationic species. In addition, a series of different gases (N<sub>2</sub>, O<sub>2</sub>, CO, CO<sub>2</sub>, C1-C4 hydrocarbons) were tested through the use of adsorption microcalorimetry in order to understand the interactions and selectivity of **1**. This study affords an in-depth approach to the characterization of a new selective adsorbent for pollutants of industrial interest.

### Introduction

Metal-Organic Frameworks (MOFs) have proven to be interesting materials due to their potential applications in multiple fields, such as catalysis,<sup>[1,2]</sup> biomedicine<sup>[3,4]</sup> gas storage and separation.<sup>[5,6]</sup> This is by cause of their unique structural and chemical features, which result from the combination of organic linkers coordinated to metal atoms or clusters, giving rise to open structures with potentially high pore volumes and surface areas, as well as unique opportunities for designing active sites,<sup>[7,8]</sup> stimuli responsiveness<sup>[9,10]</sup> or localized cooperative phenomena.<sup>[11]</sup>

The emergence of MOFs provides an alternative in applications such as pollutant entrainment and gas storage, extending the other commonly used classes of porous materials of activated carbons and zeolites.<sup>[12–14]</sup> For this purpose, accessible porosity and high surface areas are crucial features, with record values reported in several MOFs over the last decade.<sup>[15–17]</sup> However, a large uptake is not the singular requirement, as there are other relevant properties necessary such as selectivity and regenerability.<sup>[18]</sup> Here MOFs hold special promise due to their ability to be designed through the judicious choice of metal centers and corresponding linkers in order to tune their local

properties and tailor them for selective adsorption or separation.<sup>[19]</sup>

Despite their attractive properties, MOFs have been held back from industrial applications largely because of their poor chemical and thermal stability.<sup>[20,21]</sup> Extensive efforts are being made, from the design to the preparation stages, in order to improve these weak points.<sup>[22,23]</sup> One of the possible approaches in achieving this objective is by using inorganic and organic building blocks of known stability, in order to synthesize inherently more stable MOFs. A good example of such stable organic building blocks are metalloporphyrins, multifunctional biomolecules which are found in complexes, playing essential biochemical, enzymatic, and photochemical functions, based on the special properties of the tetrapyrrolic macrocycle.<sup>[24]</sup> Metalloporphyrins are remarkable precursors in supramolecular chemistry, giving rise to a variety of functional materials because of their unique chemical, physical and biological properties.<sup>[25–27]</sup>

In the wide horizons of MOFs, metalloporphyrin frameworks rouse intensive research interest, although they are still in their premature stage. Since Kosal et al. reported the first porphyrin-based MOF, PIZA-1, with a high selectivity to guest solvent molecules,<sup>[28]</sup> similar materials have reported great results in several applications areas.<sup>[29]</sup> Despite the fact that surface areas for porphyrin-based materials are average for a porous compound, the chemical features of the pyrrole ring, combined with their high stability, provide porphyrin-based MOFs optimal pore environments and surface affinity for selective adsorption and separation via thermodynamic<sup>[30]</sup> or kinetic means.<sup>[31]</sup> Moreover, the use of porphyrins as main ligands for MOFs offer the possibility to include differing open metal sites than those that coordinate between these units,<sup>[32]</sup> furthering the choices

<sup>a</sup> Department of Mineralogy and Petrology, University of the Basque Country (UPV/EHU), Sarriena 48940, Leioa, Spain.

<sup>b</sup> MADIREL UMR 7246, Aix-Marseille University, CNRS, 13397 Marseille, France.

<sup>c</sup> BCMaterials, Basque Center for Materials, Applications and Nanostructures Bld. Martina Casiano, 3rd Floor, UPV/EHU Science Park, 48940, Leioa, Spain.

<sup>d</sup> Department of Inorganic Chemistry, University of the Basque Country (UPV/EHU), Sarriena 48940, Leioa, Spain.

†Electronic Supplementary Information (ESI) available: See DOI: 10.1039/x0xx00000x

available to the skilled chemist to create multifunctional materials.

The work herein focuses on the 3D porphyrin-based MOF  $[\text{Ni}_5(\text{H}_2\text{TCPP})_2\text{O}(\text{H}_2\text{O})_4] \cdot n\text{S}$  (where TCPP is meso-tetra(4-carboxyphenyl)porphyrin and S is the solvent), previously reported by our group and further referred to as **1**,<sup>[33]</sup> and its role as a selective adsorbent for several pollutants liquid or gas phase. To achieve this goal, structural thermal and magnetic characterization were first performed in order to set the basis for its adsorbent behaviour based on its structural features, followed by adsorption tests and kinetic measurements for organic dyes, and a comprehensive characterization of the gas adsorption performance using calorimetry experiments of several greenhouse gases and light hydrocarbons.

## Materials and methods

### Materials

The non-metallated meso-tetra(4-carboxyphenyl)porphyrin ( $\text{H}_6\text{TCPP}$ ), nickel(II) nitrate hexahydrate >98.5%, 1,2,4,5-benzenetetracarboxylic acid 96% ( $\text{H}_4\text{bta}$ ) and the solvents N,N-dimethylformamide 99.8% (DMF) ethanol 96% and acetone 96% were purchased from Sigma-Aldrich Co. and used as received. The synthesis procedure was previously detailed<sup>[33]</sup> and is summarised in the ESI.

### Physicochemical characterization

Thermal behaviour was studied *in-situ* using X-ray thermodiffraction on a Bruker D8 Advance Vantec diffractometer (Cu-K $\alpha$  radiation) equipped with a variable-temperature stage (Anton Paar HTK2000) with a Pt sample holder. The powder patterns were recorded in 2 $\theta$  steps of 0.0333° in the 5–27° range, counting for 0.8 s per step. Temperature was increased from ambient conditions (25 °C) to 500 °C at 15 °C min<sup>-1</sup>.

Electron paramagnetic resonance (EPR) spectra were measured on polycrystalline samples with a Bruker ELEXSYS 500 spectrometer, operating at X band, equipped with a super-high-Q resonator ER-4123-SHQ. The magnetic field was calibrated by a NMR probe and the frequency inside the cavity was determined with an integrated MW-frequency counter. Magnetic susceptibility measurements were taken in the range of 4–300 K with a Quantum Design SQUID MPMS-7T magnetometer.

Dye adsorption experiments were performed in an ethanol solution. The organic dyes selected as simulants were cationic methylene blue (**MB**), crystal violet (**CV**), anionic Congo red (**CR**), and neutral dimethyl yellow (**DY**) (structures available in Figure S4 in ESI). 10 mg of compound **1** was added into a 4 mL glass beaker containing 1 x 10<sup>-4</sup> mol·L<sup>-1</sup> of dye ethanol solution. The mixture was then left at ambient conditions for 15 days.

Sorption kinetics were investigated through UV/Vis spectrometry, measured on a CARY 5000 spectrophotometer (Varian Inc., Santa Clara, CA, USA). Calibration of solution concentration was carried out by means of absorption at selected wavelengths, as detailed in Figures S5–S8, ESI. Dye concentration throughout loading was monitored in-situ, in the absence of light at room temperature by soaking 10 mg of compound **1** in a Quartz SUPRASIL® cell with 4 mL of dye-contaminated ethanol (1 x 10<sup>-4</sup> mol·L<sup>-1</sup>) for **MB** and **CV** and (1 x 10<sup>-5</sup> mol·L<sup>-1</sup>) for **DY**. Experimental duration was 11400 min for **CV** and **DY**, and 7200 min for **MB**. The quantity of dye adsorbed by compound **1**, expressed in mmol per gram of **1** was calculated by the following equation.<sup>[34]</sup>

$$Q_{eq} = \frac{V(C_0 - C_{eq})}{m} \quad (\text{eq. 1})$$

where  $Q_{eq}$  (mmol·g<sup>-1</sup>) is the amount of adsorbed dye by compound **1**,  $C_0$  (mmol·L<sup>-1</sup>) is the initial concentration of dye in the water,  $C_{eq}$  (mmol·L<sup>-1</sup>) is the equilibrium concentration of dye remaining in the water,  $V$  (L) is the volume of the aqueous solution, and  $m$  (g) is the weight of compound **1** used.

IR spectra on pristine and dye-loaded **1** were collected on a JASCO FT/IR-6100 spectrometer at room temperature in the range of 4000–400 cm<sup>-1</sup>, in dry KBr pellets (1% of sample).

Nitrogen physisorption at 77 K was used to determine BET area.<sup>[35]</sup> Around 100 mg of sample was activated under secondary vacuum to 150 °C for 16 hours with experiments carried out on a BELmax apparatus (MicrotracBEL, Japan). BET area of the microporous solid was calculated using the rules devised by Rouquerol et al.<sup>[35,36]</sup> Accessible micropore volume was determined using the t-plot method.

Gas adsorption isotherms and enthalpies at 303 K were measured simultaneously using a Tian-Calvet type microcalorimeter coupled with a home-made manometric gas dosing system.<sup>[37]</sup> The analyte is introduced into the system using a step-by-step method and each dose is allowed to stabilize in a reference volume before being brought into contact with the adsorbent located in the microcalorimeter. The introduction of the adsorbate to the sample is accompanied by an exothermic thermal signal, measured by the thermopiles of the microcalorimeter. The peak in the calorimetric signal is integrated to obtain the total energy released during this adsorption step. At low coverage, the error in the signal can be estimated to around  $\pm 0.2$  kJ·mol<sup>-1</sup>. Around 0.4 g of sample was outgassed at 150 °C for 16 hours under secondary vacuum prior to each experiment. For each injection, equilibrium was assumed to have been reached after 90 minutes. This was confirmed by the return of the calorimetric signal to its baseline (<5  $\mu\text{W}$ ). All laboratory-grade gases were obtained from Air Liquide. All IAST multicomponent adsorption simulations were performed using pyGAPS.<sup>[38]</sup>

## ARTICLE

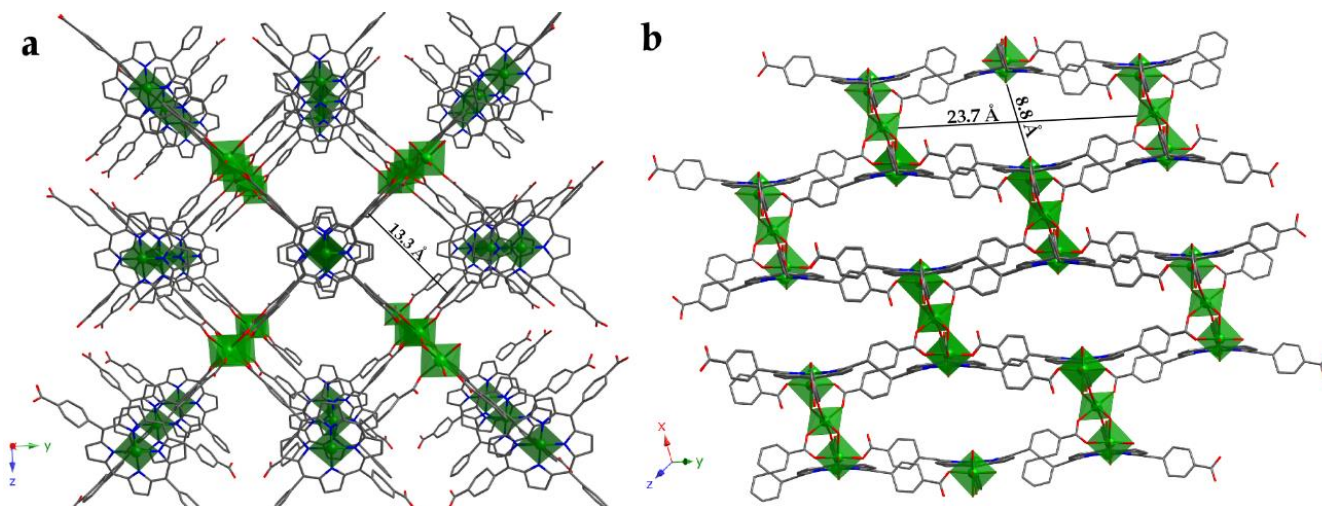


**Figure 1.** a) [100] view of 3D framework of compound **1** showing the 13.3 Å x 13.3 Å channels, and b) [112] view showing the second type of channels (23.7 Å x 8.8 Å) in crystal structure of **1**. (Ni: green, C: grey, N: dark blue, O: red). H atoms have been omitted for clarity.

## Results and Discussion

### Thermal Analysis

The structure of **1** with the formula  $[\text{Ni}_5(\text{H}_2\text{TCPP})_2\text{O}(\text{H}_2\text{O})_4] \cdot n\text{S}$  was previously reported.<sup>[33]</sup> In short, **1** crystallizes in the  $C2/m$  space group, with Ni-tetrapyrrolic units in a square planar coordination environment linked by centrosymmetric trinuclear complexes of octahedrally coordinated Ni atoms, giving rise to a 3D structure with two interconnected channels (Figure 1). After synthesis, the voids are occupied by solvent as DMF and water molecules, which can be removed through heating above 150 °C.

In order to further confirm the thermal stability of compound **1** following the previously reported thermogravimetric and differential scanning calorimetry (DSC) analysis,<sup>[33]</sup> we employed thermodiffraction, recorded on a powdered sample collected immediately after synthesis. The diffraction spectra (Figure S1 in ESI) show a small peak which is removed at 50 °C leading us to think about the presence of impurity easily removable at low temperatures. Compound **1** retains crystallinity after removal of the guest molecules, as evidenced by the presence of discrete peaks beyond 150 °C. However, above this temperature, the characteristic reflections begin to shift, indicating changes in the structure. Unfortunately, the decrease in crystallinity at high temperatures prevented an indexing of the evolution of cell parameters. Nevertheless, comparing simulated XRD pattern of **1** and the pattern registered at 160 °C in thermodiffraction (Figure S2 in ESI)

it can be observed that the most characteristic reflections of 1 experimental and simulated **1** clearly fit better than low temperature patterns. This suggests that **1** suffers slight changes in its structure with the removal of the coordinated DMF and water molecules, approaching to the structural model previously reported<sup>[33]</sup> at a higher temperature. Considering that 67% of the electron density was assigned to removable solvates during structure resolution,<sup>[33]</sup> such changes are not surprising. In addition, previous IR spectroscopy results, alongside high resolution TEM images of activated compound **1** confirm the framework backbone remains stable up to 250 °C, with a slight deviation of the lattice.<sup>[33]</sup> Above 350 °C, the structure collapses, forming a residue which has been identified by X-ray powder diffraction as NiO [S. G. Fm-3m,  $a = 4.17$  Å].<sup>[39]</sup>

### Magnetic analysis

Owing to the Ni<sup>II</sup> trinuclear moieties present in compound **1**, magnetic susceptibility measurements and EPR spectroscopy were able to be used for further characterization. The thermal evolution of the  $\chi_m^{-1}$  and  $\chi_m T$  curves is shown in Figure S3 in ESI. The molar magnetic susceptibility  $\chi_m$ , is inversely dependent on temperature throughout the studied range. Above 20 K the susceptibility follows a Curie–Weiss law [ $\chi_m = C_m / (T - \theta)$ ], with values of the Curie and Curie–Weiss constants of 6.09  $\text{cm}^3 \cdot \text{K} \cdot \text{mol}^{-1}$  and 3.8 K, respectively. The  $\chi_m T$  value at room temperature is 6.17  $\text{cm}^3 \cdot \text{K} \cdot \text{mol}^{-1}$ , close to expected for five isolated  $S=1$  Ni<sup>II</sup> ions with only a second order orbital contribution to the magnetic moment (6.05  $\text{cm}^3 \cdot \text{K} \cdot \text{mol}^{-1}$ , considering  $g=2.20$ ). When the sample is cooled, the  $\chi_m T$  product undergoes a continuous increase reaching a value of

9.68 cm<sup>3</sup>·K·mol<sup>-1</sup> at 2.2 K. This result and the small positive Weiss temperature indicate the existence of weak ferromagnetic exchange interactions in this compound in the whole measured range.

Since the crystal structure of compound **1** shows the presence of two well-isolated Ni<sup>II</sup> ions in tetrapyrrolic units and a Ni<sup>II</sup> trinuclear cluster, we have fitted the magnetic properties of this compound to a model of a S=1 linear trimer with an additional paramagnetic contribution from two S=1 isolated centers (eq. 2).

$$\chi_m = 2\chi_m(\text{mono}) + \chi_m(\text{tri}) \quad (\text{eq. 2})$$

The first term is calculated assuming a purely paramagnetic behavior obeying a Curie-law (eq. 3):

$$\chi_m(\text{mono}) = (2Ng_m^2\beta^2/3kT) \quad (\text{eq. 3})$$

In the second term, the magnetic exchange in a centrosymmetric S=1 trimer is described by the Heisenberg Hamiltonian (eq. 4).

$$H = -2J[S_1S_2 + S_2S_3] - 2J_{13}(S_1S_3) \quad (\text{eq. 4})$$

where J and J<sub>13</sub> represent the exchange coupling between neighboring and terminal ions, respectively. In the absence of a clear exchange pathway between non-neighboring ions, J<sub>13</sub> is usually taken as zero in this type of systems.<sup>[40]</sup> Thus, the following analytical expression for the magnetic susceptibility of the trimer can be derived using the van Vleck equation (eq. 5):

$$\chi_m(\text{tri}) = (2Ng_t^2\beta^2/3kT)(3 + 42e^{4x} + 15e^{2x} + 18e^{-2x} + 3e^{-6x}) / (3 + 7e^{4x} + 5e^{2x} + 8e^{-2x} + e^{-4x} + 3e^{-6x}) \quad (\text{eq. 5})$$

where  $x = J/kT$ .

The best least-squares fit (solid line in Figure S3 in ESI) was obtained with the following set of parameters:  $g_m = 2.15$ ,  $g_t = 2.22$ ,  $J/k = 6.1$  K (4.2 cm<sup>-1</sup>), with a reliability factor  $R = 4.5 \times 10^{-5}$  ( $R = \sqrt{\sum[\chi_m T^{\text{exp}} - \chi_m T^{\text{cal}}]^2 / \sum[\chi_m T^{\text{exp}}]^2}$ ).

An additional proof of the ferromagnetic coupling present in this compound is provided by the EPR spectra registered at low temperature. It is well known that octahedrally coordinated Ni<sup>II</sup> ions are usually silent in X-band EPR spectroscopy due to the rather large zero-field splitting (ZFS) of the <sup>3</sup>A<sub>2</sub> ground state.<sup>[41]</sup> However, compound **1** exhibits a broad intense EPR signal near zero-field at 4.2 K (Figure 2). The intensity of the absorption line decreases with increasing temperature following a Curie-Weiss law similar to that observed for the magnetic susceptibility (Figure 2), being  $\theta = 4$  K. This behavior indicates that the observed EPR signal corresponds to an allowed transition ( $\Delta M_s = \pm 1$ ) within the S=3 ground state, with lower ZFS than the nickel ions inside the porphyrinic units. Above 150 K the signal becomes undetectable because of its low intensity and the short spin-lattice relaxation time of Ni<sup>II</sup>.

The observed weak ferromagnetic interaction can be explained considering the angle of the oxygen bridges between two

neighboring Ni<sup>II</sup> ions, which is close to 118°. It is worth mentioning that this is a higher value compared to typical values found in literature.<sup>[42]</sup>

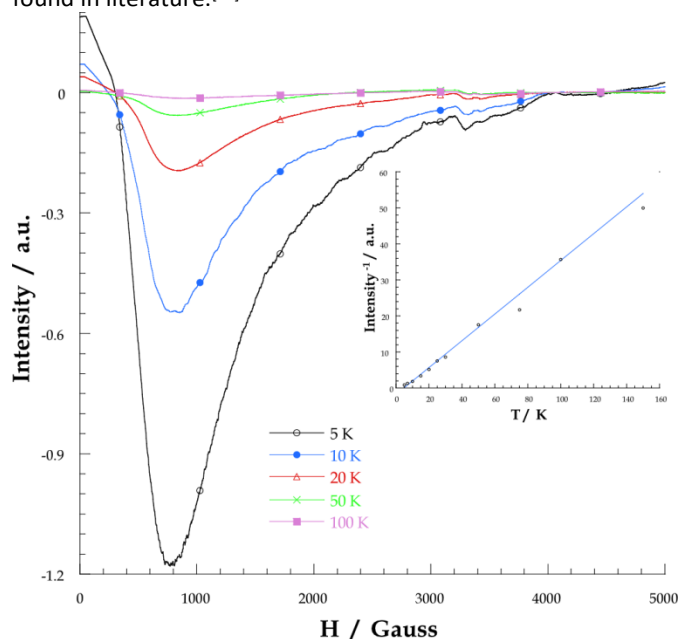


**Figure 2.** X-band EPR spectra of compound **1** registered at several temperatures. Inset shows the thermal evolution of the intensity of the EPR signal.

### Dye adsorption

We now turn to investigating the potential of **1** for several applications. Organic dyes are prevalent in many industries, including medicine, textile, leather, printing and plastic.<sup>[43]</sup> and have emerged as soils and water pollutants, media in which they remain for long periods of time due to their stability.<sup>[44–46]</sup> Due to the promise of MOFs as porous materials for their capture,<sup>[47],[48]</sup> we investigated the dye adsorption properties of compound **1** on four of the most commonly used organic dyes (Figure 3). Typically, 10 mg of **1** were soaked in a vial with 4 mL of dyes in 1 × 10<sup>-4</sup> mol·L<sup>-1</sup> ethanolic solution and left for 15 days. To the naked eye, the colour of the solutions changed to clearer after that period of time in the case of **MB**, **CV** and slightly in the case of **DY**. No changes were observable in the case of **CR**.

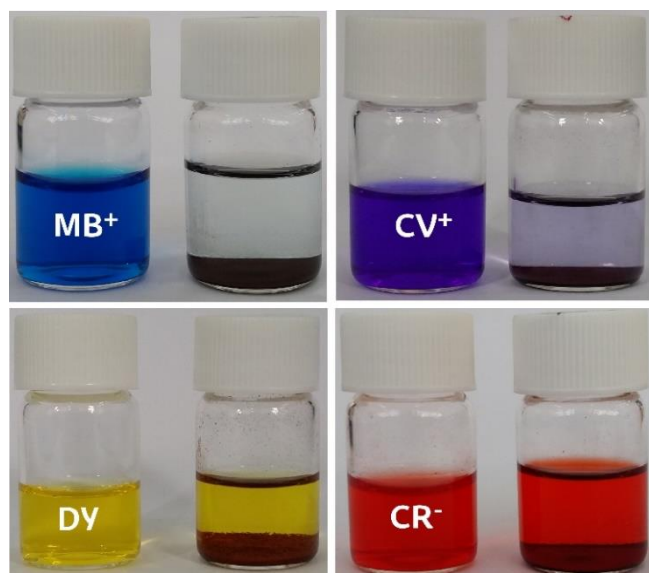


**Figure 3.** Colour changes of dye solutions of methylene blue (MB), crystal violet (CV), anionic Congo red (CR), and neutral dimethyl yellow (DY). All photos were taken after 15 days since the addition of compound **1**.

Dye adsorption was confirmed by IR spectroscopy for **MB** and **CV** (Figure S9 in ESI). For these loaded samples of compound **1**, a widening of the band at  $1580\text{ cm}^{-1}$  can be observed, which can be assigned to a greater presence of C=N bonds. Additionally, for samples loaded with **MB**, a band can be observed at  $1150\text{ cm}^{-1}$ , associated with C-S bonds. The presence of these bands in the IR spectra confirms the successful immobilization of **MB** and **CV** into the porous structure. **DY** characteristic IR bands could not be determined due to the low amount of adsorbed dye, alongside the similar bond nature between **DY** and compound **1**.<sup>[49]</sup> As represented in the adsorption histogram (Figure S10 in ESI), 1 mg of **1** can adsorb 85 mmol (25.58 mg) of **MB**, 2 mmol (0.45 mg) of **DY**, and 54 mmol (22.03 mg) of **CV**. No uptake amount was found for **CR**.

The kinetics of adsorption studied via in-situ UV-Vis spectroscopy are presented in Figure S11 in ESI, with a two-step process visible. The first is very rapid, while the second one is much slower. It is noteworthy to specify that for **MB** and **CV** the adsorption process gradually continues after the measured time, while for **DY** the adsorption stabilizes after 24 h. Adsorption kinetics were adjusted to a first order model, being the best fitting model for this adsorption performance. Due to the presence of two kinetic regimes, adsorption rate constants were calculated for the first step where most of the adsorption has taken place. Thus, calculated adsorption rate constants for **MB**, **CV**, and **DY** are  $1.2 \times 10^{-2}$ ,  $3.3 \times 10^{-3}$  and  $7 \times 10^{-4}\text{ min}^{-1}$ , respectively (Figure S12 in ESI).

In order to put these results in context, a comparison has been made with the adsorbed amounts by some known porous materials for cationic MB (as is the most reported in the field and the dye with the highest amount adsorbed by **1** under similar conditions to those of this work.

Table 1. Comparison of capacities of adsorption of MB on different adsorbents

Adsorbent	Dye	$Q_{eq}$ (mg·g <sup>-1</sup> )	$K_1$ (min <sup>-1</sup> )/ $K_2$ (g/mg·min)	Ref.
<b>1</b>	MB	25.58	$1.2 \times 10^{-2}$ / -	This work
HKUST-1	MB	29.5	-/-	[50]
MOF-235	MB	100	-/9.58x10 <sup>-5</sup>	[51]
Amino-MIL-101 (Al)	MB	380	$7 \times 10^{-2}$ / $2.6 \times 10^{-3}$	[52]
Chitosan-clay composite	MB	26.93	$2.1 \times 10^{-3}$ / $2.1 \times 10^{-2}$	[53]
Graphene oxide	MB	39.92	$1.4 \times 10^{-2}$ / $9 \times 10^{-4}$	[54]
Carbon nanotubes	MB	24	-/-	[55]

Despite the fact that **1** is not among the highest adsorption capacity values reported for other well-known MOFs, this compound exhibits a remarkable adsorption capacity towards MB comparable to other porous materials,

It is worth mentioning that the molecular dimensions of **MB**, **CV** and **DY** are in the size range of the square pore (Figure 1), whereas **CR** is much larger in width and length. The different kinetics of adsorption can be rationalised as the synergy among the dye shapes (Figure S4 in ESI), dimensions (Table S1 in ESI) and ionic strength,<sup>[56,57]</sup> likely conditioned by weakly ferromagnetic interactions in Ni<sup>II</sup> trinuclear complexes. Thus, cationic **MB** and **CV** were adsorbed by compound **1**, while anionic **CR** and neutral **DY** adsorption were null or negligible. Adsorption of **MB** was higher and faster than for **CV**, due to the fact that **MB** molecular size is smaller than **CV** and can fit properly in the square pores of compound **1** (1.3 nm wide). This leads us to postulate that dye adsorption of compound **1** is more effective for cationic and small molecules, as in the case of methylene blue. This result clearly indicates that **1** could effectively and selectively adsorb dye molecules based on the charge and size-exclusion effect, which makes it a promising candidate for application in dye removal and fluid treatment.

#### Gas adsorption

All adsorption measurements were carried out with samples outgassed at 150 °C to ensure a complete removal of solvent from the pore network. The nitrogen accessible surface area at 77 K is found to be  $388\text{ m}^2\cdot\text{g}^{-1}$  (Figure S13 in ESI), lower than crystallographically expected (over  $1000\text{ m}^2\cdot\text{g}^{-1}$  assumed from the high void space in the lattice), indicating that some structural changes occur upon activation. Such effects are often encountered in porphyrin-based MOFs, with the surface area of the reference isostructural PIZA-1<sup>[28]</sup> found to be three times lower than **1** after activation. As elucidated through thermal analysis, compound **1** shows subtle differences in its high temperature diffractogram (shifted characteristic peaks). The observed evolution likely accounts for some of the morphological surface changes, although we know from other techniques (FTIR and HRTEM)<sup>[33]</sup> that the framework remains stable.

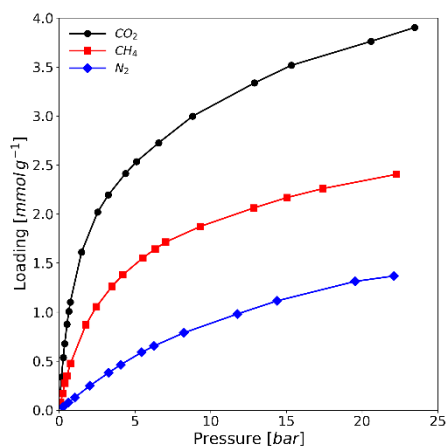


Figure 4. Gas adsorption isotherms for CO<sub>2</sub>, CH<sub>4</sub>, and N<sub>2</sub> at 303 K.

Ambient temperature (303 K) adsorption manometry was performed at high pressure with nine probes (N<sub>2</sub>, O<sub>2</sub>, CO, CO<sub>2</sub>, CH<sub>4</sub>, C<sub>2</sub>H<sub>6</sub>, C<sub>3</sub>H<sub>8</sub>, C<sub>3</sub>H<sub>6</sub>, C<sub>4</sub>H<sub>10</sub>), chosen for their differing physicochemical properties as well as for their potential industrial interest. Selected isotherms are presented in Figure 4 and 5, with the complete dataset of adsorption isotherms for each of the probes used available in Figures S16–S18 in ESI.

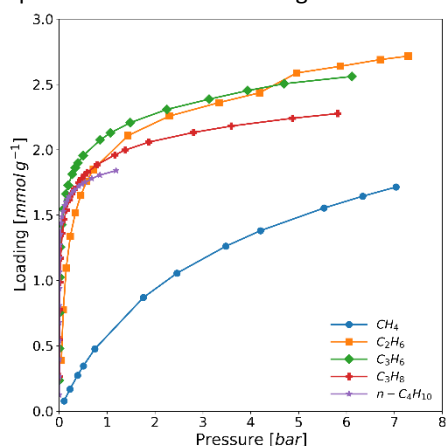


Figure 5. Gas adsorption isotherms for C1–C4 hydrocarbons at 303 K.

All isotherms can be identified as Langmuir type I, with varying degrees of affinity to the framework due to the strength of the guest–host interaction. N<sub>2</sub>, O<sub>2</sub> and CO isotherms are nearly linear, hinting to non-specific adsorption sites and weak attraction to the pore walls of **1**. CO<sub>2</sub>, with its quadrupolar nature, has a much stronger affinity, reflected in the steep isotherm slope at low pressure. The slope is also observed to become sharper with the increase of the carbon number of the hydrocarbon series, as expected from the longer interacting chain of the probe molecule.

To further understand these interactions, adsorption microcalorimetry was employed. The surface properties of compound **1** can be investigated through direct measurement of the differential enthalpy of adsorption as a function of loading. While the recorded curve is a sum of all possible interactions within the system (both guest–host and guest–guest

contributions) the shape of the curve can be still be rationalised. In **1**, it is expected that the Ni atoms coordinated at the centre of the porphyrin ligands may be able to act as sorption sites, interacting with adsorbed guests through the axial position, which should appear as a heterogenous profile in the enthalpy curve. The resulting experimental curves (with CO<sub>2</sub>, CH<sub>4</sub>, CO and C<sub>3</sub>H<sub>8</sub> depicted in Figure 6 and other probes in Figures S16–S18 in ESI) do not suggest this to be the case, with the material displaying an unexpected surface homogeneity. Enthalpy profiles were either completely flat throughout the entire adsorption range or slowly decreasing as guest–guest interactions took over and further rearrangement of adsorbed molecules is required to completely fill the pores.

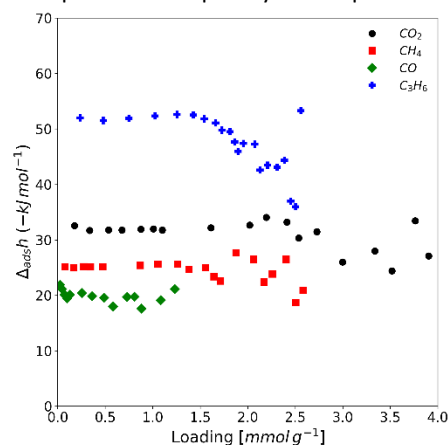


Figure 6. Differential enthalpy of adsorption as a function of amount adsorbed for four adsorbents which have the potential to interact differently with the open metal site in **1**: CO<sub>2</sub>, CH<sub>4</sub>, CO and C<sub>3</sub>H<sub>6</sub>.

The differential enthalpy of adsorption at zero coverage does not point to any specific interactions with any of the used probes. For carbon dioxide this value (31 kJ·mol<sup>-1</sup>) is close to other MOFs with Ni and Cu open metal sites, such as Ni-STA-12<sup>[58]</sup> (35 kJ·mol<sup>-1</sup>) and HKUST-1<sup>[59]</sup> (32 kJ·mol<sup>-1</sup>), yet lower than zeolite NaX (49 kJ·mol<sup>-1</sup>) or MIL-100(Fe) (39 kJ·mol<sup>-1</sup>), which are known to have specific CO<sub>2</sub> adsorption sites. Carbon monoxide in particular, with its sorption enthalpy of 20 kJ·mol<sup>-1</sup>, does not show evidence of porphyrin metal centre coordination. On the other hand, the initial adsorption enthalpy for methane is higher than prototypical MOFs and NaX zeolite, and comparable to Takeda 5A activated carbon.<sup>[59]</sup> This may suggest an effect from the framework itself, either through pore confinement or favourable stacking of molecules.

In terms of capacity, as assessed from uptake at 1 bar and 20 bar, **1** is seen to compare favourably to several conventional adsorbent families of industrial interest. These values are summarised in Table 1, alongside literature data for a microporous activated carbon molecular sieve, two zeolites and HKUST-1 MOF. It can be seen that **1** shows a lower-than-average capacity for CO<sub>2</sub>, around 1.2 mmol·g<sup>-1</sup> at 1 bar, and up to 4 mmol·g<sup>-1</sup> at 20 bar. In comparison, the carbon dioxide adsorption capacity for Takeda 5A and zeolite 13X are both higher, around 8 mmol·g<sup>-1</sup> and 7.6 mmol·g<sup>-1</sup> at 20 bar, respectively, while HKUST-1 is significantly higher at 13 mmol·g<sup>-1</sup>

<sup>1</sup>. Other adsorbates follow similar trends as CO<sub>2</sub>, with uptakes on **1** roughly halved proportional to the microporous Takeda 5A. While the total uptake is lower than these reference materials, the more process relevant working capacity (WC) between these two pressures is seen to rival that of the zeolites at ~1.5 mmol·g<sup>-1</sup>.

**Table 1.** Uptakes of CO<sub>2</sub>, N<sub>2</sub> and CH<sub>4</sub> at 1 bar and 20 bar for **1**. Relevant reference adsorbents are included for comparison.

Adsorbent	CO <sub>2</sub> (mmol/g)		N <sub>2</sub> (mmol/g)		CH <sub>4</sub> (mmol/g)		Ref.
	1	20	1	20	1	20	
pressure (bar)							
<b>1</b>	1.2	3.7	0.2	1.4	0.5	2.4	This work
HKUST-1	5	13	0.3	2.2	1.1	5	[60]
Takeda 5A	2	8	0.3	2.6	0.9	4.7	[61]
Zeolite 13X	5	7.6	0.3	2	0.9	3.8	[60]
Zeolite NaX	4.7	6.5	/	/	0.5	3.6	[60]

Ideal adsorbed solution theory (IAST) calculations were carried out to assess the potential of **1** for mixture separation. The calculations had industrially relevant mixtures as model inputs: (i) 10% CO<sub>2</sub> in N<sub>2</sub> as post-combustion flue gas simulant, (ii) an equimolar mixture of propylene and propane paraffin/olefin separation and (iii) a 1:1 ratio of carbon dioxide and methane as a common blend encountered in many natural gas deposits. The IAST-predicted selectivity is presented in Table 1 and compared to three relevant compounds.

**Table 1.** IAST calculated selectivity for compound **1** for three common binary mixtures, at 1 bar and at 5 bar. Some reference materials are included for comparison.

Adsorbent	Com. 1	Com. 2	%1	Selectivity (1 bar)	Selectivity (5 bar)	Ref.
<b>1</b>	CO <sub>2</sub>	N <sub>2</sub>	10	19.0	19.2	This work
<b>1</b>	CO <sub>2</sub>	CH <sub>4</sub>	50	3.2	3.6	This work
<b>1</b>	C <sub>3</sub> H <sub>6</sub>	C <sub>3</sub> H <sub>8</sub>	50	1.4	1.5	This work
Takeda 5A	CO <sub>2</sub>	N <sub>2</sub>	10	19	/	[59]
Takeda 5A	CO <sub>2</sub>	CH <sub>4</sub>	50	/	4	[59]
HKUST-1	CO <sub>2</sub>	N <sub>2</sub>	10	19	/	[59]
HKUST-1	CO <sub>2</sub>	CH <sub>4</sub>	50	/	7	[59]
Zeolite NaX	CO <sub>2</sub>	CH <sub>4</sub>	10	/	212	[59]

Selectivities for **1** are seen to be in the range of 19-19.5 for the CO<sub>2</sub>/N<sub>2</sub> mixture, 3-4 for CO<sub>2</sub>/CH<sub>4</sub>, and slightly above unity for propane/propylene. For the former two mixtures, selectivities are comparable to those of the microporous carbon and the HKUST-1 MOF. However, they pale in comparison to those of

Zeolite NaX, where strong CO<sub>2</sub> interactions are known to efficiently sequester it from a mixture.

Full composition range adsorbed-gas phase selectivity curves for each pair of gases chosen have also been generated, as shown in Figure S19 in ESI. It can be seen that the curves do not vary much with pressure, as previously suggested from the flat enthalpy profile for the mixture component gases. It should be noted that these selectivity values represent equilibrium results, with kinetic-based sieving likely able to play a role given the microporous nature of **1** and should be investigated in a further study. Overall, **1** is seen to most resemble the Takeda 5A activated carbon in its sorption behaviour, further motivating the general homogenous surface and flat enthalpy curves previously recorded.

## Conclusions

In summary, the structural arrangement of the 3D porphyrin-based compound **1** exhibit crystallochemical features that result in several properties of interest, such as its weakly ferromagnetic interactions between Ni<sup>II</sup> ions and its permanent accessible surface area with open pores. As such, compound **1** has been tested and found to be a promising selective adsorbent for pollutants in solution and for energy-pertaining gases. For simulant dye pollutants in ethanol solution, our results confirm that the ferromagnetic compound **1** exhibits affinity for cationic dyes, as in the case of **MB** blue and **CV**. The channels in its crystal structure allow the entrance of guest molecules, albeit with possible steric hindrance for very large dyes. It is worth mentioning that **1** reduces the concentration of **MB** blue in ethanol more than 10 times in 15 days, a remarkable value comparable with other adsorbents in literature. Regarding gas adsorption, the various probes used in this work confirm its remarkable adsorption capacity, comparable with other known MOFs and activated carbons. In addition, adsorption enthalpies measured through calorimetry reveal a homogeneous surface chemistry of **1** in the adsorption process, which indicate no specific interactions with these probes. Finally, IAST calculations predict promising selectivity for the separation of CO<sub>2</sub> in N<sub>2</sub>, C<sub>3</sub>H<sub>6</sub> in C<sub>3</sub>H<sub>8</sub> and CO<sub>2</sub> in CH<sub>4</sub>. These characteristics make **1** a great example of multifunctionality of porphyrin-based MOFs and encourage the community to study further the structure versatility of these materials in order to discover their numerous applications.

## Conflicts of interest

There are no conflicts to declare.

## Acknowledgements

This work has been financially supported by the "Ministerio de Economía, Industria y Competitividad" (MAT2016-76739R) (AEI/FEDER, EU) and the "Gobierno Vasco" (Basque University System Research Groups, IT-1290-19) and the University of the Basque Country (GIU18/197) which are gratefully acknowledge.

The technical and human support provided by SGIker (UPV/EHU) is gratefully acknowledged. The MADIREL authors received funding from the European Union's Horizon 2020 research and innovation program, under the Marie Skłodowska-Curie grant agreement No 641887 (project acronym: DEFNET).

## Notes and references

- [1] Y. B. Huang, J. Liang, X. S. Wang, R. Cao, *Chemical Society Reviews* **2017**, *46*, 126–157.
- [2] P. Cancino, A. Vega, A. Santiago-Portillo, S. Navalon, M. Alvaro, P. Aguirre, E. Spodine, H. García, *Catalysis Science and Technology* **2016**, *6*, 3727–3736.
- [3] P. Horcajada, R. Gref, T. Baati, P. K. Allan, G. Maurin, P. Couvreur, G. Férey, R. E. Morris, C. Serre, *Chemical Reviews* **2012**, *112*, 1232–1268.
- [4] M. C. Bernini, D. Fairen-Jimenez, M. Pasinetti, A. J. Ramirez-Pastor, R. Q. Snurr, *Journal of Materials Chemistry B* **2014**, *2*, 766–774.
- [5] Z. Bao, G. Chang, H. Xing, R. Krishna, Q. Ren, B. Chen, *Energy and Environmental Science* **2016**, *9*, 3612–3641.
- [6] N. Sikdar, A. Hazra, T. K. Maji, *Inorganic Chemistry* **2014**, *53*, 5993–6002.
- [7] J. Lee, O. K. Farha, J. Roberts, K. A. Scheidt, S. T. Nguyen, J. T. Hupp, *Chemical Society Reviews* **2009**, *38*, 1450–1459.
- [8] Y.-B. Huang, J. Liang, X.-S. Wang, R. Cao, *Chemical Society Reviews* **2017**, *46*, 126–157.
- [9] G. Férey, *Chemical Society Reviews* **2008**, *37*, 191–214.
- [10] A. Schneemann, V. Bon, I. Schwedler, I. Senkovska, S. Kaskel, R. A. Fischer, *Chemical Society Reviews* **2014**, *43*, 6062–6096.
- [11] T. M. McDonald, J. A. Mason, X. Kong, E. D. Bloch, D. Gygi, A. Dani, V. Crocellà, F. Giordanino, S. O. Odoh, W. S. Drisdell, B. Vlasisavljevich, A. L. Dzubak, R. Poloni, S. K. Schnell, N. Planas, K. Lee, T. Pascal, L. F. Wan, D. Prendergast, J. B. Neaton, B. Smit, J. B. Kortright, L. Gagliardi, S. Bordiga, J. A. Reimer, J. R. Long, *Nature* **2015**, *519*, 303–308.
- [12] K. T. Chue, J. N. Kim, Y. J. Yoo, S. H. Cho, R. T. Yang, *Industrial and Engineering Chemistry Research* **1995**, *34*, 591–598.
- [13] J. L. Soares, H. J. José, R. F. P. M. Moreira, in *Brazilian Journal of Chemical Engineering, Assoc. Brasileira De Eng. Química / Braz. Soc. Chem. Eng.*, **2003**, pp. 75–80.
- [14] E. Díaz, E. Muñoz, A. Vega, S. Ordóñez, *Chemosphere* **2008**, *70*, 1375–1382.
- [15] H. Li, M. Eddaoudi, M. O’Keeffe, O. M. Yaghi, *Nature* **1999**, *402*, 276–279.
- [16] O. K. Farha, I. Eryazici, N. C. Jeong, B. G. Hauser, C. E. Wilmer, A. A. Sarjeant, R. Q. Snurr, S. T. Nguyen, A. Ö. Yazaydin, J. T. Hupp, *Journal of the American Chemical Society* **2012**, *134*, 15016–15021.
- [17] H. Furukawa, N. Ko, Y. B. Go, N. Aratani, S. B. Choi, E. Choi, A. Ö. Yazaydin, R. Q. Snurr, M. O’Keeffe, J. Kim, O. M. Yaghi, *Science* **2010**, *329*, 424–428.
- [18] S. Bourrelly, P. L. Llewellyn, C. Serre, F. Millange, T. Loiseau, G. Férey, *Journal of the American Chemical Society* **2005**, *127*, 13519–13521.
- [19] J. R. Li, R. J. Kuppler, H. C. Zhou, *Chemical Society Reviews* **2009**, *38*, 1477–1504.
- [20] J. J. Low, A. I. Benin, P. Jakubczak, J. F. Abrahamian, S. A. Faheem, R. R. Willis, *Journal of the American Chemical Society* **2009**, *131*, 15834–15842.
- [21] P. Guo, D. Dutta, A. G. Wong-Foy, D. W. Gidley, A. J. Matzger, *Journal of the American Chemical Society* **2015**, *137*, 2651–2657.
- [22] H. Cui, Y. Wang, Y. Wang, Y. Z. Fan, L. Zhang, C. Y. Su, *CrystEngComm* **2016**, *18*, 2203–2209.
- [23] C. Wang, X. Liu, N. Keser Demir, J. P. Chen, K. Li, *Chemical Society Reviews* **2016**, *45*, 5107–5134.
- [24] K. M. Kadish, K. M. Smith, R. Guilard, W. S. (Firm), **2012**, 229.
- [25] Y. Ke, D. J. Collins, H. C. Zhou, *Inorganic Chemistry* **2005**, *44*, 4154–4156.
- [26] M. Heidari-Golafzani, M. Rabbani, R. Rahimi, A. Azad, *RSC Advances* **2015**, *5*, 99640–99645.
- [27] B. J. Burnett, P. M. Barron, W. Choe, *CrystEngComm* **2012**, *14*, 3839–3846.
- [28] M. E. Kosal, J. H. Chou, S. R. Wilson, K. S. Suslick, *Nature Materials* **2002**, *1*, 118–121.
- [29] W. Y. Gao, M. Chrzanowski, S. Ma, *Chemical Society Reviews* **2014**, *43*, 5841–5866.
- [30] A. Fateeva, S. Devautour-Vinot, N. Heymans, T. Devic, J. M. Grenèche, S. Wuttke, S. Miller, A. Lago, C. Serre, G. De Weireld, G. Maurin, A. Vimont, G. Férey, *Chemistry of Materials* **2011**, *23*, 4641–4651.
- [31] P. G. Boyd, A. Chidambaram, E. García-Díez, C. P. Ireland, T. D. Daff, R. Bounds, A. Gładysiak, P. Schouwink, S. M. Moosavi, M. M. Maroto-Valer, J. A. Reimer, J. A. R. Navarro, T. K. Woo, S. Garcia, K. C. Stylianou, B. Smit, *Nature* **2019**, *576*, 253–256.
- [32] C. Wang, D. Liu, W. Lin, *Journal of the American Chemical Society* **2013**, *135*, 13222–13234.

- [33] E. Amayuelas, A. Fidalgo-Marijuán, B. Bazán, M. K. Urriaga, G. Barandika, M. I. Arriortua, *CrystEngComm* **2017**, *19*, 7244–7252.
- [34] G. Crini, *Dyes and Pigments* **2008**, *77*, 415–426.
- [35] J. Rouquerol, F. Rouquerol, P. Llewellyn, G. Maurin, K. Sing, *Adsorption by Powders and Porous Solids - 2nd Edition*, **2013**.
- [36] J. Rouquerol, P. Llewellyn, F. Rouquerol, *Studies in Surface Science and Catalysis* **2007**, *160*, 49–56.
- [37] P. L. Llewellyn, G. Maurin, *Comptes Rendus Chimie* **2005**, *8*, 283–302.
- [38] P. Iacomì, P. L. Llewellyn, *Adsorption* **2019**, *25*, 1533–1542.
- [39] S. R. Batten, N. R. Champness, X. Chen, J. Garcia-martinez, S. Kitagawa, L. Öhrström, M. O. Keeffe, M. P. Suh, J. Reedijk, *Pure Appl. Chem.* **2013**, *85*, 1715–1724.
- [40] L. M. Callejo, G. Madariaga, L. Lezama, L. Fidalgo, N. De La Pinta, R. Cortés, *Inorganic Chemistry* **2010**, *49*, 5353–5355.
- [41] R. L. Carlin, R. L. Carlin, in *Magnetochemistry*, Springer Berlin Heidelberg, **1986**, pp. 19–35.
- [42] P. Mukherjee, M. G. B. Drew, V. Tangoulis, M. Estrader, C. Diaz, A. Ghosh, *Inorganic Chemistry Communications* **2009**, *12*, 929–932.
- [43] G. Crini, *Bioresource Technology* **2006**, *97*, 1061–1085.
- [44] C. Zou, Z. Zhang, X. Xu, Q. Gong, J. Li, C. De Wu, *Journal of the American Chemical Society* **2012**, *134*, 87–90.
- [45] M. A. Al-Ghouti, M. A. M. Khraisheh, S. J. Allen, M. N. Ahmad, *Journal of Environmental Management* **2003**, *69*, 229–238.
- [46] L. Zhou, C. Gao, W. Xu, *ACS Applied Materials and Interfaces* **2010**, *2*, 1483–1491.
- [47] E. M. Dias, C. Petit, *Journal of Materials Chemistry A* **2015**, *3*, 22484–22506.
- [48] Q. Gao, J. Xu, X. H. Bu, *Coordination Chemistry Reviews* **2019**, *378*, 17–31.
- [49] E. Amayuelas, A. Fidalgo-Marijuán, B. Bazán, M.-K. Urriaga, G. Barandika, M.-I. Arriortua, *CrystEngComm* **2016**, *18*, DOI 10.1039/c5ce02511g.
- [50] X. Zhao, S. Liu, Z. Tang, H. Niu, Y. Cai, W. Meng, F. Wu, J. P. Giesy, *Nature Publishing Group* **2015**, DOI 10.1038/srep11849.
- [51] E. Haque, J. W. Jun, S. H. Jung, *Journal of Hazardous Materials* **2011**, *185*, 507–511.
- [52] E. Haque, V. Lo, A. I. Minett, A. T. Harris, T. L. Church, **2014**, DOI 10.1039/c3ta13589f.
- [53] M. Auta, B. H. Hameed, *Chemical Engineering Journal* **2014**, *237*, 352–361.
- [54] T. Liu, Y. Li, Q. Du, J. Sun, Y. Jiao, G. Yang, Z. Wang, Y. Xia, W. Zhang, K. Wang, H. Zhu, D. Wu, *Colloids and Surfaces B: Biointerfaces* **2012**, *90*, 197–203.
- [55] Y. Yao, F. Xu, M. Chen, Z. Xu, Z. Zhu, *Bioresource Technology* **2010**, *101*, 3040–3046.
- [56] Q. K. Liu, J. P. Ma, Y. Bin Dong, *Chemical Communications* **2011**, *47*, 12343–12345.
- [57] M. B. Dewal, M. W. Lufaso, A. D. Hughes, S. A. Samuel, P. Pellechia, L. S. Shimizu, *Chemistry of Materials* **2006**, *18*, 4855–4864.
- [58] S. R. Miller, G. M. Pearce, P. A. Wright, F. Bonino, S. Chavan, S. Bordiga, I. Margiolaki, N. Guillou, G. Férey, S. Bourrelly, P. L. Llewellyn, *Journal of the American Chemical Society* **2008**, *130*, 15967–15981.
- [59] V. Benoit, R. S. Pillai, A. Orsi, P. Normand, H. Jobic, F. Nouar, P. Billefont, E. Bloch, S. Bourrelly, T. Devic, P. A. Wright, G. De Weireld, C. Serre, G. Maurin, P. L. Llewellyn, *Journal of Materials Chemistry A* **2016**, *4*, 1383–1389.
- [60] Z. Liang, M. Marshall, A. L. Chaffee, *Energy & Fuels* **2009**, *23*, 2785–2789.
- [61] A. D. Wiersum, C. Giovannangeli, D. Vincent, E. Bloch, H. Reinsch, N. Stock, J. S. Lee, J.-S. Chang, P. L. Llewellyn, *ACS Combinatorial Science* **2013**, *15*, 111–119.